GEOPHYSICS, VOL. 86, NO. 3 (MAY-JUNE 2021); P. S235–S245, 11 FIGS.
10.1190/GEO2020-0364.1

Addressing the crosstalk issue in imaging using seismic multiple wavefields

Shaoping Lu[1], Lingyun Qiu[2], and Xiang Li[3]

ABSTRACT

Surface-related-multiple wavefields constitute redundant information in conventional migration and can often be difficult to attenuate. However, when used for migration, multiple wavefields can improve subsurface illumination. Unfortunately, the process of imaging using multiples involves the management of crosstalk, which largely restricts its application. Crosstalk causes phantom images formed by spurious correlation of unrelated events in a migration process. These events can be unrelated orders of multiples in the source and receiver wavefields; they can also be one event associated with a reflector in the source wavefield and another event generated by a different reflector in the receiver wavefield. We have first examined crosstalk by explicitly investigating its generation mechanisms in a migration process and classifying it into different categories based on causality. Following this analysis, crosstalk can be predicted in a migration process and subtracted in the image domain; however, this method is usually difficult to apply due to the complexity of wavefield separation and adaptive subtraction. Furthermore, we develop different algorithms to attenuate the crosstalk, including a deconvolution imaging condition, a least-squares migration (LSM) method, and an advanced algorithm combining LSM with a deconvolution imaging condition. We evaluate these different strategies with synthetic examples. A deconvolution imaging condition can attenuate some crosstalk, but it is less effective at suppressing strong coherent crosstalk events. However, the LSM method can fundamentally address the crosstalk issue, and this approach is further optimized when combined with a deconvolution imaging condition.

INTRODUCTION

In seismic data processing, surface-related multiples are often treated as redundant information and are removed before migration (Verschuur, 1991). Instead of being discarded, surface-related multiples can be treated as signals to image the subsurface. There are different strategies proposed for imaging multiple wavefields, and each has advantages and limitations. The main approaches include the up-down wavefield imaging method (Berkhout and Verschuur, 1994), seismic interferometry (Schuster and Rickett, 2000), and Marchenko imaging (Wapenaar et al., 2014).

Berkhout and Verschuur (1994) propose the concept of imaging using multiples and implement the idea by using the up-down wavefield imaging principle. Because this approach follows the same migration procedure (Claerbout, 1971) as primary imaging, it is straightforward to adopt conventional methods, such as anisotropic and viscoelastic wavefield imaging and angle gather computation algorithms, to image with multiples. Therefore, this approach is appropriate for industrial implementations and has been developed to establish mature migration tools for practical applications (Lu et al., 2015). However, this strategy has some limitations such as the generation of crosstalk from either unrelated orders of multiples or from different reflection events. This is because when surface data are used as source and receiver wavefields, imaging of multiples is a natural blending migration algorithm that automatically generates crosstalk. Moreover, based on the sampling theory, the source wavefield at the boundary must be sampled properly according to the Nyquist frequency; this can be a substantial challenge when applied

Manuscript received by the Editor 5 June 2020; revised manuscript received 20 January 2021; published ahead of production 6 February 2021; published online 21 April 2021.
[1]Sun Yat-Sen University, School of Earth Sciences and Engineering, No. 135 Xingangxi Road, Guangzhou, Guangdong 510275, China and Southern Marine Science and Engineering Guangdong Laboratory (Zhuhai), Zhuhai, Guangdong 519000, China. E-mail: lushaoping@mail.sysu.edu.cn (corresponding author).
[2]Tsinghua University, Yau Mathematical Sciences Center, Beijing 100084, China and Yanqi Lake Beijing Institute of Mathematical Sciences and Applications, Beijing 101408, China. E-mail: lyqiu@tsinghua.edu.cn.
[3]CNPC BGP Inc., Houston, Texas 77043, USA. E-mail: jw.li.xiang@gmail.com.

to streamer data, for which the cable separation can be up to 100 m. In addition, because the approach by Berkhout and Verschuur (1994) is based on the up-down wavefield imaging principle, its implementation is mostly suitable with wave-equation migration (WEM) algorithms, such as the one-way WEM or the reverse time migration (Liu et al., 2011) methods.

By crosscorrelating the data, seismic interferometry extracts the wave lag between two seismometers. Schuster and Rickett (2000) use the stationary-phase theory to demonstrate that the migration of these extracted data, which are multiple wavefields, can generate an image of the subsurface. In fact, seismic interferometry converts multiple wavefields into primary wavefields. This method can be used in many circumstances, such as global seismology and explorational geophysics. Analogously, Shan (2003) proposes an approach to convert surface multiples into pseudoprimaries by crosscorrelating the seismic data at the surface. The advantage of this method is that, after the pseudoprimaries are generated, any conventional algorithm can be used for further processing. However, the computational cost is a bottleneck of this method. When pseudoprimaries are generated, a new shot gather is created at each receiver location, resulting in a large volume of data. Therefore, the cost of forming and imaging the pseudoprimaries is high, which restricts the real application of this algorithm.

Multiple migration can also be applied using the Marchenko imaging principle (Wapenaar et al., 2014), which estimates Green's functions between a subsurface reflection measurement and a surface location. In contrast to the interferometry approach, the virtual sources and receivers can be present in the subsurface. Therefore, the Marchenko algorithm can image surface and interbed multiples. The Marchenko imaging algorithm can be implemented by applying redatuming; thus, it can avoid the crosstalk generated by internal multiples in the overburden. However, this approach relies on the subsurface properties, which restricts its application in real scenarios (Ravasi et al., 2016).

Although the imaging of multiples can be performed using different algorithms, it involves crosstalk formed by unrelated events, which largely prevents this technique from being applied in practice. To address the crosstalk issue, various approaches have been applied, such as migration with a deconvolution imaging condition (Valenciano and Biondi, 2003; Guitton et al., 2007; Muijs et al., 2007; Lu et al., 2015), imaging with controlled-order multiples (Liu et al., 2016), angle gather Radon crosstalk suppression (Wang et al., 2014; Wong et al., 2015), crosstalk prediction and attenuation using migration (Lu et al., 2016), and least-squares migration (LSM) (Tu et al., 2013; Berkhout, 2014; Ordoñez et al., 2014; Zhang and Schuster, 2014; Wong et al., 2015; Davydenko and Verschuur, 2016; Liu et al., 2016; Lu et al., 2018a).

Migration with a deconvolution imaging condition attenuates certain crosstalk, and it is convenient to apply in the frequency domain using one-way WEM, for which different strategies have been implemented and investigated (Valenciano and Biondi, 2003; Guitton et al., 2007; Muijs et al., 2007; Lu et al., 2015). However, a deconvolution imaging condition can partially suppress crosstalk because the true inverse of the forward process is not established.

A strong component of the crosstalk is generated by the interference between unrelated orders of multiples; thus, imaging controlled-order multiples can avoid this type of crosstalk (Liu et al., 2016). However, crosstalk may remain in the image when more than one reflector exists in the model. In addition, this approach requires the successful separation of different orders of multiple wavefields, which usually is computationally intensive and challenging to implement.

When imaging with multiples, the crosstalk issue can be investigated in prestack images, i.e., common image gathers. When crosstalk events are generated, their angle gathers display different moveouts with variations in angle. Mathematically, the trajectory of crosstalk events in angle gathers can be calculated and crosstalk can be predicted and attenuated in the angle domain (Wang et al., 2014; Wong et al., 2015). However, this approach is difficult to apply in practice. For instance, for small angles, the moveout of crosstalk events decreases whereas their amplitude increases, which makes them very difficult to suppress. In addition, in practice, the moveout of angle gathers is affected by velocity errors, which adds complexity to the prediction and attenuation of crosstalk in this domain.

Crosstalk can be calculated by applying a migration process with proper combinations of source and receiver wavefields (Lu et al., 2016). Theoretically, we can compute their phase components, which correspond to the positions of the crosstalk events. To attenuate these events, an adaptive subtraction process is needed, but this process is technically nontrivial. In addition, the effectiveness of this algorithm relies on the ability to separate multiple wavefields from primary fields. Multiple migration involves crosstalk because of its adjoint property with the forward process. Instead, LSM computes the inverse of the forward extrapolation process; therefore, it should address the crosstalk issue. However, an inversion solution may converge slowly or diverge when iteratively suppressing crosstalk.

Although different strategies have been proposed to address the crosstalk problem, a fundamental theoretical investigation and a mathematical derivation of the problem are still needed. In the following sections, we revisit the forward, adjoint, and inverse processes of seismic wavefield propagation to investigate imaging algorithms that use multiples, examine the crosstalk issue associated with these methods, and address the issue using different approaches.

THEORY

Crosstalk phenomena in the imaging of multiples

In this section, we explain the origin of crosstalk when multiples are used for imaging. In conventional migration, a controlled wavelet, i.e., a transient signal, is used to generate the source wavefield to image the primaries. Mathematically, the source and receiver wavefields can be defined as

$$S = G_s S_0, \quad R = G_r R_1, \tag{1}$$

where S is the source wavefield generated from a point source S_0 with a forward propagation operator G_s (Green's function) and R is the receiver wavefield computed from the primary wavefield R_1 using a backpropagation operator G_r (Green's function).

When imaging multiples, instead of isolating the individual order of multiple events, we choose to use the downgoing and upgoing components in the recorded seismic data as the source and receiver wavefields, respectively, and we simultaneously image all of the multiple wavefields together. The source and receiver wavefields can be computed as

$$S = \left(G_s \sum_j S_j\right), \quad R = \left(G_r \sum_l R_l\right), \tag{2}$$

where S_j is the jth-order downgoing wavefield and R_l is the lth-order upgoing wavefield at the recording surface (Figure 1). Then, the imaging of multiples can be performed using either a cross-correlation (equation A-1) or a deconvolution imaging condition (equation A-2).

To better understand the crosstalk problem, we rewrite the imaging conditions explicitly with a plane-wave solution. We choose a 2D model with a constant velocity v_0, a reflector at depth Z_m (with reflectivity m), and a free surface at $Z = 0$ m, which can create surface multiples (Figure 1). By solving the acoustic wave equation A-3, we can compute the pressure wavefield P at depth z (equation A-6).

In Figure 1, we label the wavefields before and after they are reflected at depth Z_m and at the surface. The term S_0 is an impulse source wavefield, D_0 is the downgoing incidence wavefield at the reflector, U_0 is the reflected upgoing wavefield at the reflector, and R_1 is the receiver wavefield at the surface, which is associated with the first bounce of the subsurface reflection, i.e., the primary wavefield. However, due to the reflection at the free surface, the primary wavefield R_1 is reflected downward and acts as a secondary source wavefield. We label this wavefield S_1, the corresponding downgoing and upgoing wavefields D_1 and U_2, and the receiver wavefield R_2, which is the first-order multiple. Analogously, we label the higher order multiples as S_j, D_j, U_j, and R_j (Figure 1).

We assume that the free-surface reflection coefficient is equal to -1, and in a plane-wave sense, the above wavefields can be explicitly formulated as

$$S_j = (-1)^j m^j S_0 \exp[(-ik_z)2jz], \tag{3}$$

$$D_j = (-1)^j m^j S_0 \exp[(-ik_z)(2j+1)z], \tag{4}$$

$$U_j = (-1)^{j-1} m^j S_0 \exp[(-ik_z)(2j-1)z], \tag{5}$$

$$R_j = (-1)^{j-1} m^j S_0 \exp[(-ik_z)2jz]. \tag{6}$$

In general, all surface multiples can be used for migration by applying equation A-1, and the imaging result can be estimated as

$$I_{\text{corr}} = \sum_{\omega} \left[\sum_{l} \sum_{j} (-1)^{j+l-1} m^{j+l} |S_0|^2 \exp[(-ik_z)2(l-(j+1))z] \right]. \tag{7}$$

In equation 7, we focus on evaluating the phase terms $(-ik_z)2(l-(j+1))z$ of the image. In these terms, when $l = j+1$, equation 7 produces an image of the reflector. However, if $l \neq j+1$, the corresponding terms are present at incorrect positions, and these terms generate crosstalk. Compared to the true reflectivity m, the crosstalk terms have extra lags of $(-ik_z)2(l-(j+1))z$ in terms of phase differences. When $n = l-(j+1)$ is positive, the corresponding events appear at deeper positions than the true reflectors, and these events are referred to as nth-order "causal crosstalk." In Figure 2a, when reflector 1 is imaged by wavefield U_2^1, this wavefield also creates an event (dashed blue) at a deeper position than reflector 1, and it is a causal crosstalk event associated with reflector 1. However, if n is negative, the corresponding events are advanced by phase differences $-ik_z 2nz$. Therefore, ghost images appear at positions shallower than their true locations. This phenomenon seems to contradict the causality; thus, these events are called $|n|$th-order "anticausal crosstalk." In Figure 2b, when reflector 2 is imaged by wavefield U_1^2, this wavefield also creates an event (dashed black) at a shallower position than itself, and it has an associated anticausal crosstalk event. The classification of causal and anticausal crosstalk is defined based on the positions relative to their corresponding true reflector. Therefore, the causality is obvious for the simple layered model in Figure 2. For a more realistic scenario, where consecutive reflectors exist, the crosstalk interferes with real events; even though the crosstalk events are still causal and anticausal with respect to their corresponding real reflector locations, they can appear anywhere in the imaging domain and be challenging to differentiate.

The objective of classifying causal and anticausal crosstalk is not to remove them based on their causalities, but to better understand their generation mechanism. The causal and anticausal crosstalk events can be calculated independently, and we investigate the algorithm of crosstalk estimation in the following section.

Crosstalk estimation

We can estimate the crosstalk by a migration process. However, instead of calculating their true amplitude, we focus on estimating their phase. To image causal crosstalk, we use a point source S_0 as the source wavefield and the multiple model $R_l (l > 1)$ to establish the receiver wavefields. The causal crosstalk $I_{\text{c-prediction}}$ can be predicted as

$$I_{\text{c-prediction}} = \sum_{\omega} \sum_{l>1} (-1)^{l-1} m^l S_0^2 \exp[(-ik_z)2(l-1)z]. \tag{8}$$

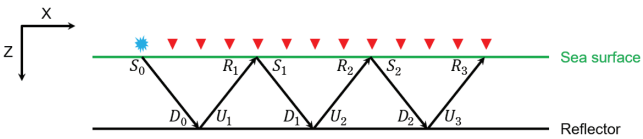

Figure 1. A 2D model (with constant velocity) and the trajectory of a single plane wave.

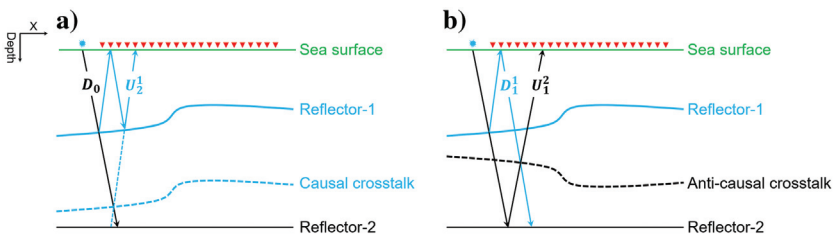

Figure 2. A two-reflector model for displaying causal and anticausal crosstalk events. In (a), D_0 is the downgoing wavefield from the point source, and U_2^1 is the first-order multiple wavefield from reflector-1. In (b), D_1^1 is the first-order downgoing wavefield generated from reflector-1 and reflected by the sea surface, and U_1^2 is the upgoing primary wavefield generated from reflector-2.

Because $l-1$ is always larger than zero, equation 8 involves only causal crosstalk events without either the true image or anticausal crosstalk terms. Analogously, we can predict the anticausal crosstalk. We use all the wavefields $S_j(j>0)$ as the source wavefield and the primary wavefield $R_l(l=1)$ as the receiver wavefield. Then, the anticausal crosstalk $I_{\text{a-prediction}}$ can be calculated as

$$I_{\text{a-prediction}} = \sum_{j>0}(-1)^j m^{1-j} S_0^2 \exp[(-ik_z)2(-j)z]. \quad (9)$$

Because $j>0$, the phase $(-ik_z)2(-j)z$ in equation 9 comprises all negative elements of equation 7, which are all the anticausal crosstalk events without the real image and causal crosstalk terms.

In summary, we can calculate the positions of all causal and anticausal crosstalk events using the proper source and receiver wavefields. First, to compute the causal crosstalk, we need the multiple wavefields. Then, to compute the anticausal crosstalk, we need the primary wavefields. Therefore, performing crosstalk estimation requires surface-related-multiple elimination.

Imaging of multiples with a deconvolution imaging condition

Mathematically, the forward process can be represented as a modeling operator $\mathbf{L}$, and it maps the singularity in the reflectivity to its analog in the data. When we use a crosscorrelation imaging condition (equation A-1) in migration, we apply the adjoint operator $\mathbf{L}^*$, which is a low-computational-cost substitution of the inverse operator $\mathbf{L}^{-1}$ without considering amplitude accuracy. This motivates the use of a deconvolution-based imaging condition (equation A-2), in which the operator $\mathbf{L}_d^*$ not only shares the same kinematic behavior as $\mathbf{L}^*$ but also provides more accurate amplitude information.

The deconvolution imaging condition in equation A-2 can be rewritten as

$$I_{\text{decon}} = \sum_{\omega} \frac{\left(\sum_j D_j^*\right)\left(\sum_l U_l\right)}{\left(\sum_j D_j^*\right)\left(\sum_j D_j\right)}, \quad (10)$$

and the crosscorrelation imaging condition in equation A-1 can be rewritten as

$$I_{\text{corr}} = \left(\sum_j D_j^*\right)\left(\sum_l U_l\right). \quad (11)$$

For the imaging of primaries, a controlled wavelet is used as the source wavefield and the primary data are used as the receiver wavefield, which means that we set $j=0$ and $l=1$ in equations 10 and 11, respectively. For the simple model in Figure 1, the source and receiver wavefields can be computed based on equations 3–6. Then, the output from using a crosscorrelation imaging condition becomes

$$I_{\text{corr}} = S_0^2 m, \quad (12)$$

and the output from using a deconvolution imaging condition is

$$I_{\text{decon}} = m. \quad (13)$$

Therefore, when imaging primaries, a deconvolution imaging condition removes the source signature and produces an image with more accurate phase and amplitude than a crosscorrelation imaging condition, which is useful for computing true amplitude images (Zhang et al., 2005).

For the imaging of multiples, there exists a great number of combinations when conducting the imaging condition by forward- and backward-extrapolated wavefields with different orders of multiples. These combinations can generate true events, but many of them are crosstalk. A deconvolution imaging condition can attenuate certain crosstalk and partially address the crosstalk issue.

To thoroughly examine the effect of a deconvolution imaging condition on crosstalk attenuation, we explicitly decompose equations 10 and 11. Based on the derivation in Appendix B, the image from the crosscorrelation imaging condition can be expressed as

$$I_{\text{corr}} = S_0^2 \sum_j m^{2j+1} + S_0^2 I_c + S_0^2 I_a, \quad (14)$$

and the image from the deconvolution imaging condition simplifies to

$$I_{\text{decon}} = \sum_{\omega} \frac{S_0^2 \sum_j m^{2j+1} + S_0^2 I_c + S_0^2 I_a}{S_0^2 \sum_j m^{2j} + S_0^2 I_d} \approx m + \sum_{\omega} \frac{A_0}{1+B_0}, \quad (15)$$

where A_0 and B_0 are defined in equation B-7.

Equation 14 shows that the image from multiples using a crosscorrelation imaging condition I_{corr} is contaminated by the source signature S_0 and strong crosstalk (I_c and I_a). In contrast, equation 15 shows that the image of a deconvolution imaging condition I_{decon} is not affected by the source signature S_0, and it computes a result with amplitude m plus a small term. This is because when data are used as the source wavefield in multiple imaging, this signal is a coda. Within a certain time window, this coda behaves as a source signature that can be deconvolved by an imaging condition in equation 15 (Muijs et al., 2007). Therefore, a deconvolution imaging condition is particularly effective at attenuating the short-period crosstalk. Moreover, in the imaging of multiples with a crosscorrelation imaging condition, the impact of the source signature varies in images of different orders of multiples, which makes certain orders of multiples easily dominate the imaging result and produce crosstalk events as strong as the signal component (equation 14). In contrast, a deconvolution imaging condition makes each order of multiple produce the signal component with the same amplitude (equation 15). Therefore, the signal components from each order of multiple are stackable, which produces an image with a better signal-to-noise ratio than a crosscorrelation imaging condition, which effectively attenuates crosstalk.

Imaging of multiples with least-squares migration

To further correct the error associated with the low-computational-cost substitution $\mathbf{L}^*$ and the improved operator $\mathbf{L}_d^*$, we can use an optimization approach to obtain an accurate approximation of $\mathbf{L}^{-1}$:

$$\mathbf{m}_{\text{ls}} = \underset{m}{\text{argmin}} \frac{1}{2}\|\mathbf{d}_{\text{obs}} - \mathbf{L}\mathbf{m}\|_2^2. \quad (16)$$

This process is often referred to as LSM, in which $\mathbf{d}_{\text{obs}}$ is the observed seismic data at the receivers, and $\mathbf{m}_{\text{ls}}$ is the least-squares solution.

The traditional migration solution is given by

$$\mathbf{m}_{\text{im}} = \mathbf{L}^{*}\mathbf{d}_{\text{obs}}. \tag{17}$$

It has been demonstrated that $\mathbf{m}_{\text{ls}}$ has much less crosstalk than $\mathbf{m}_{\text{im}}$ (Lu et al., 2018a). Note that crosstalk dominates the error in the imaging result. Thus, we can write

$$\mathbf{m}^{+} \approx \mathbf{m}_{\text{im}} - \mathbf{m}_{\text{xtalk}}, \tag{18}$$

where $\mathbf{m}^{+}$ is the true reflectivity; hence, the receiver wavefield $\mathbf{d}_{\text{obs}} = \mathbf{L}\mathbf{m}^{+}$. The term $\mathbf{m}_{\text{xtalk}}$ represents the artifacts caused by crosstalk. Based on equation 18, it follows that

$$\begin{aligned}
\mathbf{m}_{\text{ls}} - \mathbf{m}_{\text{im}} &= \underset{m}{\text{argmin}}\frac{1}{2}\|\mathbf{d}_{\text{obs}} - \mathbf{L}\mathbf{m} - \mathbf{L}\mathbf{m}_{\text{im}}\|_2^2,\\
\mathbf{m}_{\text{ls}} &= \mathbf{m}_{\text{im}} + \underset{m}{\text{argmin}}\frac{1}{2}\|\mathbf{L}\mathbf{m}^{+} - \mathbf{L}(\mathbf{m} + \mathbf{m}_{\text{im}})\|_2^2,\\
\mathbf{m}_{\text{ls}} &= \mathbf{m}_{\text{im}} + \underset{m}{\text{argmin}}\frac{1}{2}\|\mathbf{L}\mathbf{m}_{\text{xtalk}} + \mathbf{L}\mathbf{m}\|_2^2.
\end{aligned} \tag{19}$$

Here, the process for the minimization problem $\underset{m}{\text{argmin}}\frac{1}{2}\|\mathbf{L}\mathbf{m}_{\text{xtalk}} + \mathbf{L}\mathbf{m}\|_2^2$ is to approximate $\mathbf{m}_{\text{xtalk}}$ in a least-squares sense and its output is used to correct $\mathbf{m}_{\text{im}}$. In other words, when using $\mathbf{m}_{\text{im}}$ as the initial model in LSM, all of the remaining iteration steps aim to attenuate the crosstalk. Therefore, when convergence is achieved, crosstalk is suppressed.

Based on equation 15, the deconvolution imaging condition cannot thoroughly address the crosstalk issue. However, equation 19 shows that the iteration steps in an LSM with multiples can minimize the crosstalk effects. We demonstrate the iterative crosstalk attenuation process using LSM in the "Examples" section.

Least-squares migration of multiples using a deconvolution imaging condition

Because a deconvolution imaging condition can suppress certain crosstalk, we integrate it with LSM for the imaging of multiples. First, we generalize the traditional least-squares problem into a weighted form:

$$\mathbf{m} = \arg\min_{m}\frac{1}{2}\|\mathbf{d}_{\text{obs}} - \mathbf{L}\mathbf{m}\|_{2,w}^2, \tag{20}$$

where the weight w in the norm (equation 20) can be chosen such that the deconvolution imaging condition is used in the migration $\mathbf{L}_d^{*}$,

$$\mathbf{m} = \arg\min_{m}\frac{1}{2}\|\mathbf{d}_{\text{obs}} - \mathbf{L}(\mathbf{L}_d^{*}\mathbf{d}_{\text{obs}})\|_2^2. \tag{21}$$

However, this minimization approach is not optimal because the forward operator $\mathbf{L}$ and reverse operator $\mathbf{L}_d^{*}$ do not form an adjoint pair. To optimize the inversion problem, we choose to adjust the LSM process by using the adjoint forward and reverse operators. Then, efficient least-squares solvers, such as conjugate gradient (CG) or least squares with QR-factorization (LSQR) method (Paige and Saunders, 1982), can be used. To obtain a solution, we apply a transformation $\mathbf{T}$ to the least-squares problem and rewrite it as

$$\begin{aligned}
\mathbf{m} &= \arg\min_{\mathbf{m}}\frac{1}{2}\|\mathbf{T}\mathbf{d}_{\text{obs}} - \mathbf{T}\mathbf{L}(\mathbf{L}_d^{*}\mathbf{d}_{\text{obs}})\|_2^2\\
&= \arg\min_{\mathbf{m}}\frac{1}{2}\|\mathbf{d}'_{\text{obs}} - \mathbf{\Lambda}(\mathbf{\Lambda}^{*}\mathbf{d}'_{\text{obs}})\|_2^2,
\end{aligned} \tag{22}$$

where $\mathbf{d}'_{\text{obs}} = \mathbf{T}\mathbf{d}_{\text{obs}}$, $\mathbf{T}\mathbf{L}(\mathbf{L}_d^{*}\mathbf{d}_{\text{obs}}) = \mathbf{\Lambda}(\mathbf{\Lambda}^{*}\mathbf{d}'_{\text{obs}})$. By applying this transformation, we have the relation

$$\mathbf{L}\mathbf{L}_d^{*} = \mathbf{\Lambda}\mathbf{\Lambda}^{*}. \tag{23}$$

Equation 23 ensures that a deconvolution imaging condition is applied and that the adjoint relation between the forward process $\mathbf{\Lambda}$ and the reverse operation $\mathbf{\Lambda}^{*}$ is maintained.

To apply the above transform, we use the following operator:

$$\mathbf{T} = \sum_{\omega}\mathbf{G}_r\frac{\mathbf{G}_r^{*}}{\sqrt{(\mathbf{G}_s\mathbf{S})^{*}(\mathbf{G}_s\mathbf{S})}}. \tag{24}$$

With this operator, the data become

$$\mathbf{d}'_{\text{obs}} = \sum_{\omega}\mathbf{G}_r\frac{\mathbf{G}_r^{*}\mathbf{d}_{\text{obs}}}{\sqrt{(\mathbf{G}_s\mathbf{S})^{*}(\mathbf{G}_s\mathbf{S})}}. \tag{25}$$

The forward process can be formulated as

$$\mathbf{\Lambda}\mathbf{m} = \sum_{\omega}\frac{(\mathbf{G}_s\mathbf{S})^{*}\mathbf{m}}{\sqrt{(\mathbf{G}_s\mathbf{S})^{*}(\mathbf{G}_s\mathbf{S})}}. \tag{26}$$

The adjoint process can be formulated as

$$\begin{aligned}
\mathbf{\Lambda}^{*}\mathbf{d}'_{\text{obs}} &= \sum_{\omega}\frac{(\mathbf{G}_s\mathbf{S})^{*}(\mathbf{G}_r^{*}\mathbf{d}'_{\text{obs}})}{\sqrt{(\mathbf{G}_s\mathbf{S})^{*}(\mathbf{G}_s\mathbf{S})}} = \sum_{\omega}\frac{(\mathbf{G}_s\mathbf{S})^{*}(\mathbf{G}_r^{*}\mathbf{d}'_{\text{obs}})}{(\mathbf{G}_s\mathbf{S})^{*}(\mathbf{G}_s\mathbf{S})}\\
&= \mathbf{L}_d^{*}\mathbf{d}_{\text{obs}},
\end{aligned} \tag{27}$$

which is migration with a deconvolution imaging condition $\mathbf{L}_d^{*}$. To stabilize the deconvolution imaging condition, we apply smoothing (Guitton et al., 2007) and add a small damping factor to the denominator (equation 27):

$$\sqrt{(\mathbf{G}_s\mathbf{S})^{*}(\mathbf{G}_s\mathbf{S})} \leftrightarrow \sqrt{\langle(\mathbf{G}_s\mathbf{S})^{*}(\mathbf{G}_s\mathbf{S})\rangle_{x,y} + \varepsilon(\mathbf{x},\omega)}, \tag{28}$$

where $\langle\rangle_{x,y}$ involves a smoothing operator applied in the space domain. Here, we use a five-point triangle smoothing operator. The term $\varepsilon(\mathbf{x},\omega)$ is a small number that varies with frequency and position.

By applying the above algorithm, we formulate an LSM with a deconvolution imaging condition $\mathbf{L}_d^{*}$. Moreover, the forward operator $\mathbf{\Lambda}$ and reverse process $\mathbf{\Lambda}^{*}$ are adjoint to each other, which is optimal for effectively solving the inverse problem.

EXAMPLES

In this section, we illustrate the imaging of multiples using the Sigsbee2b 2D synthetic model (Paffenholz et al., 2002). The synthetic

data are generated with a shot interval of 45.72 m (500 shots in total) and a receiver interval of 22.86 m (maximum offset 7932.42 m, split-spread geometry). A Ricker wavelet is used with a dominant frequency of 20 Hz and a maximum frequency of 45 Hz. The data are recorded with a sampling rate of 8 ms for 20 s and with free-surface multiples. With this data set, we demonstrate the crosstalk issue and compare different crosstalk attenuation algorithms described in the preceding sections. The following experiments can be considered as inverse crime tests, in which the migration operator is the adjoint of the modeling operator used to create the synthetic data.

The Sigsbee2b model consists of a water bottom that can generate strong multiples. In Figure 2, we examine the crosstalk phenomenon using a two-reflector model, which mimics the major reflectors in the Sigsbee2b model. Based on the analysis, we can better understand the crosstalk issue in a realistically complex model, such as Sigsbee2b. To perform the experiment, we use the up/downgoing wavefields recorded at the sea surface as inputs and apply one-way WEM to image all orders of multiples. We display the sedimentary section of the imaging results in Figure 3 and compare the results with those from the conceptual model in Figure 2. Based on our classification, in Figure 3a, the event indicated by the red arrows is causal crosstalk associated with the water-bottom reflection and the event indicated by the black arrows is anticausal crosstalk related to the bottom reflector reflection (generated by the interference between the reflections from the water bottom and the bottom reflector). Figure 3b and 3c displays the causal and anticausal crosstalk obtained using equations 8 and 9, respectively. Figure 3d shows the result after adaptively subtracting the predicted crosstalk from the raw image.

In addition to the two major reflectors, the Sigsbee2b model has many other layers, which create more crosstalk events than the two-reflector model in Figure 2. These events can be observed below the causal crosstalk associated with the water bottom in Figure 3b. Additionally, there are anticausal crosstalk events above the major anticausal crosstalk in Figure 3c. The experiment using the Sigsbee2b model shows that in a model with realistic complexity, the causal and anticausal crosstalk can be successfully estimated by using equations 8 and 9. However, instead of calculating the true amplitudes, we focus on estimating the crosstalk phases; then, we apply an adaptive subtraction approach to attenuate them. In practice, we implement the process of adaptive subtraction for each angle, where the angle gathers are computed from the migration (Figure 4). In this domain, the crosstalk events are more separable than those in a stacked image (Wang et al., 2014; Wong et al., 2015), which makes the adaptive subtraction process more effective. The proposed algorithm has been applied to real data examples (Lu et al., 2016), and it effectively attenuates strong crosstalk events.

As discussed in the preceding section, a deconvolution imaging condition partially suppresses crosstalk, whereas LSM addresses the crosstalk issue by solving an inverse problem. We perform the imaging of multiples with the deconvolution imaging condition

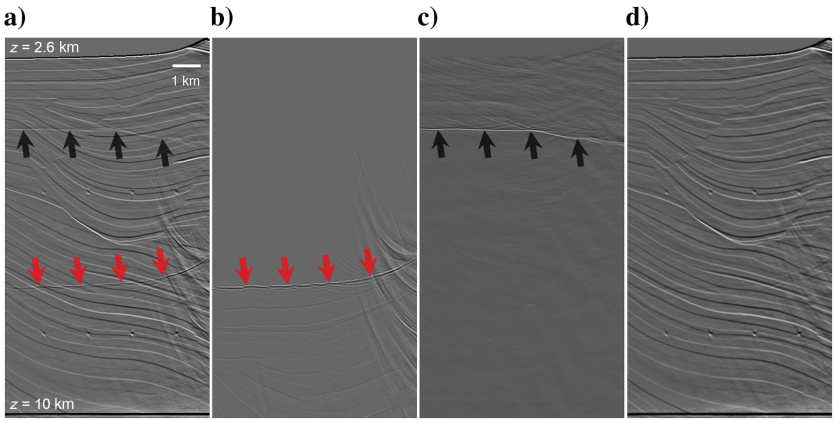

Figure 3. Imaging results from using the Sigsbee2b model (the sedimentary section). (a) Image of multiples, (b) causal crosstalk prediction, (c) anticausal crosstalk prediction, and (d) image results after adaptively removing the crosstalk. The red arrows indicate causal crosstalk, and the black arrows indicate anticausal crosstalk.

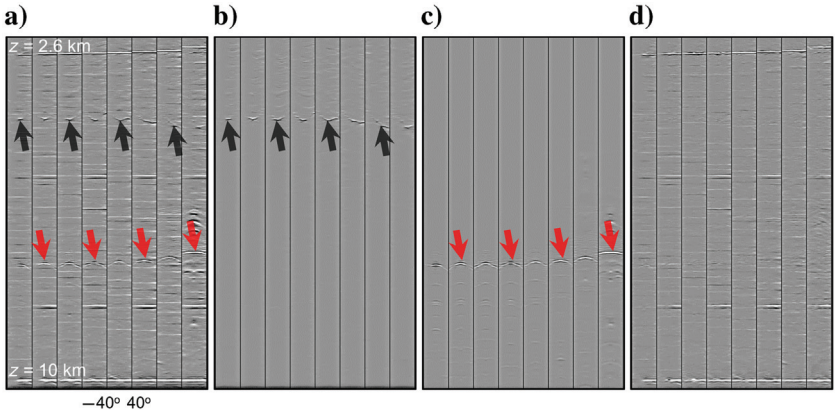

Figure 4. Angle gathers using the Sigsbee2b model (the sedimentary section): (a) raw image of multiples, (b) image of anticausal crosstalk, (c) image of causal crosstalk, and (d) image after crosstalk attenuation.

and least-squares inversion, and the results are displayed in Figures 5 and 6. Figure 5a–5c shows the full Sigsbee2b images, and Figure 6a–6c displays the corresponding results for the sediment segmentations. For comparison, the true reflectivity is displayed in Figures 5d and 6d. We can see that strong crosstalk events are present in Figures 5a and 6a, which are the images computed by using the crosscorrelation imaging condition. A deconvolution imaging condition attenuates certain short-period crosstalk in the area with complex structures (inside the red box, Figure 5b); however, it is less effective in removing the strongest crosstalk events in the sediments (Figure 6b). LSM generally yields accurate reflectivities, except in the subsalt area (Figure 5c), which is a shadow zone caused by the aperture limitation in the data.

In the imaging of primaries and multiples, the shadow zones below the salt bottom and in the lower right corner are induced by the lack of wavefield coverage. Lu et al. (2018a) demonstrate that LSM can largely mitigate these shadow zones in the imaging of primaries. In comparison, the imaging of multiples can help improve illumination, especially for shallow targets, where the wavefield coverage from multiples is much larger than that from primaries (Lu et al., 2015). However, this is not necessarily true when illuminating a deep target, where the energy of multiple wavefields, especially higher order multiples, is much less than that of primaries (Lu et al., 2018b). Therefore, the illumination of the lower right corner of Sigsbee2b from LSM with primaries (Lu et al., 2018a) is better than that from LSM with multiples (Figure 5).

We use a workflow (Figure 7) to elaborate the process of LSM with multiples. Compared to a conventional LSM workflow, LSM with multiples applies the migration and modeling using the data as the source wavefield. The effect of LSM for crosstalk attenuation has been demonstrated in equation 19, which shows that LSM iteratively suppresses crosstalk events. To demonstrate this process, we

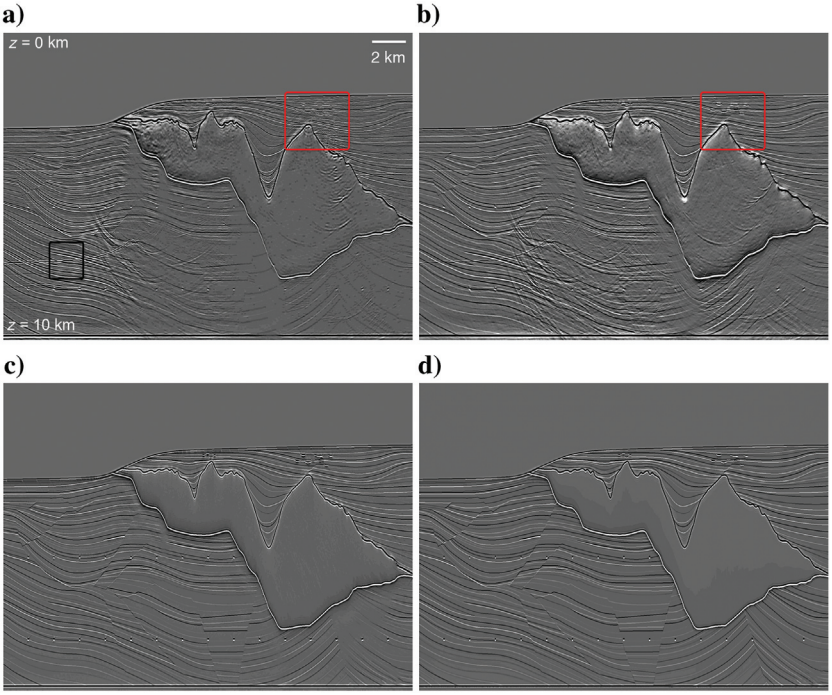

Figure 5. Imaging of multiples with (a) a crosscorrelation imaging condition, (b) a deconvolution imaging condition, (c) LSM, and (d) the true reflectivity model.

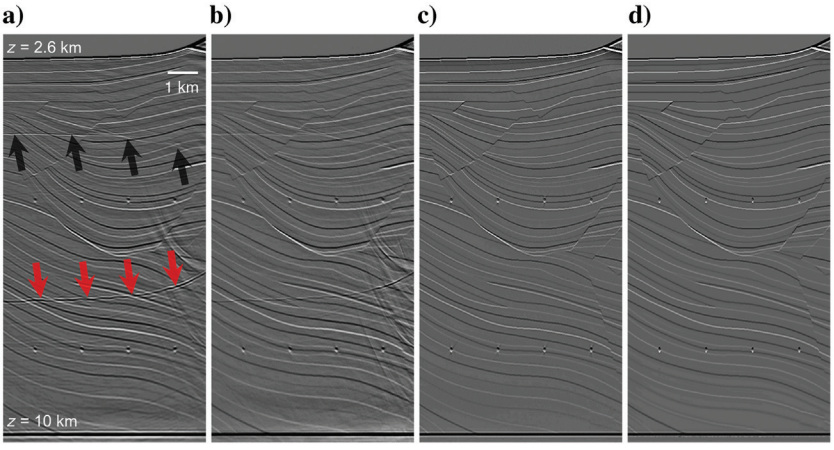

Figure 6. The sediment sections of Sigsbee2b from imaging of multiples with (a) a crosscorrelation imaging condition, (b) a deconvolution imaging condition, (c) LSM, and (d) the true reflectivity model.

display the imaging results from every fifth iteration in Figure 8: the number in the upper left corner is the iteration number and the last plot is the true reflectivity. These results are from a subsection of the Sigsbee2b model (the black box area in Figure 5), where very strong crosstalk contaminates the true reflectors. The imaging results in Figure 8 show that the LSM iteratively removes the crosstalk.

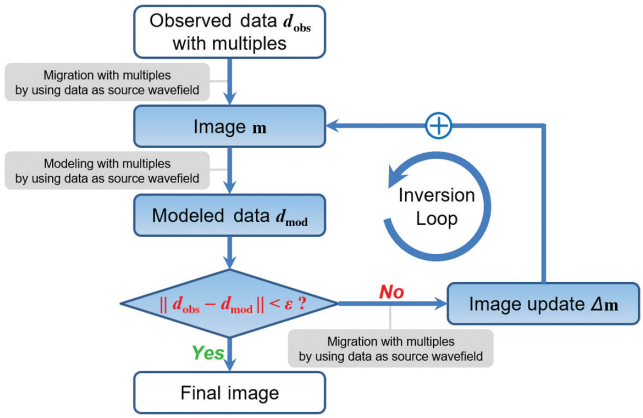

Figure 7. An iterative LSM algorithm for imaging of multiples.

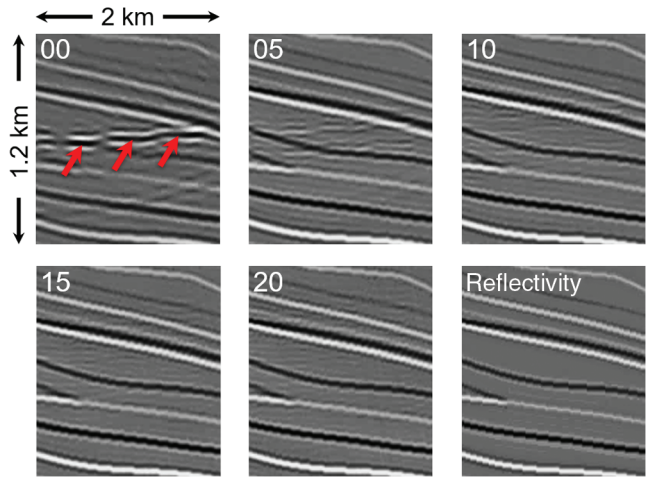

Figure 8. Imaging of multiples with LSM from Sigsbee2b (the black box segmentation in Figure 5). The number in the upper left corner is the iteration number. The last plot displays the true reflectivity.

Finally, we apply LSM with a deconvolution imaging condition (equation 22) to image multiples, and the results are displayed in Figure 9. As discussed in the preceding sections, deconvolution-based LSM should converge much more quickly and be more stable than crosscorrelation LSM. This is demonstrated by comparing the objective functions, in which the fourth iteration of deconvolution-based LSM is equivalent to the tenth iteration of crosscorrelation-based LSM; in addition, the fifth iteration of deconvolution LSM is equivalent to the 20th iteration of crosscorrelation LSM (Figure 10). Therefore, the result of the fifth iteration of deconvolution LSM (Figure 9c) is comparable with that of the 20th iteration of cross-correlation LSM (Figure 9b). However, obvious residual crosstalk still exists in Figure 9a, which is a result of the fifth iteration of crosscorrelation LSM. Figure 9d displays an image residual during LSM, which demonstrates the crosstalk attenuation achieved by LSM.

In addition to validating LSM with synthetic examples, we investigate its sensitivity to the noise level in the input data. The noise is created by normally distributed random numbers:

$$\mathbf{d}_{\mathrm{obs_noise}} = \mathbf{d}_{\mathrm{obs}} + \alpha * norm(\mathbf{d}_{\mathrm{obs}}) * \mathbf{M}_{\mathrm{randn}(m,n)}, \qquad (29)$$

where $\alpha \in [0, 1]$ controls the noise level and $\mathrm{norm}(\mathbf{d}_{\mathrm{obs}})$ is the root-mean-square of the seismic data. The dimension of the seismic data $\mathbf{d}_{\mathrm{obs}}$ is $m \times n$ and $\mathbf{M}_{\mathrm{randn}(m,n)}$ is an $m \times n$ matrix of random numbers, whose values vary from -1 to 1.

The imaging results show that LSM is sensitive to the noise level. When the noise is relatively small, i.e., $\alpha = 0.1$, LSM can still attenuate most crosstalk (Figure 11b). With the increase in the noise level, i.e., $\alpha = 0.2$, the results become noisy and, more importantly, the crosstalk is harder to remove by LSM (Figure 11c). Finally, to mimic a realistic scenario, a noninverse crime experiment is performed, in which synthetic data are generated by a different modeling operator than the one used in LSM. The results show that LSM can remove some low-amplitude crosstalk; however, there is a strong crosstalk residual in the final result (Figure 11d), which is associated with the strong water-bottom reflection.

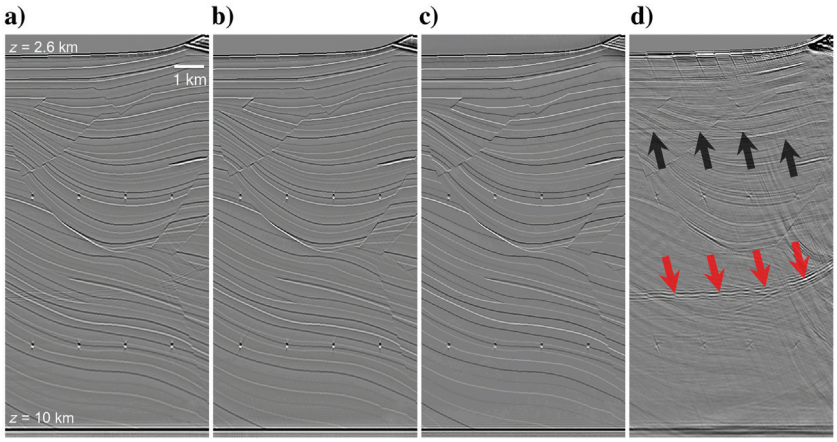

Figure 9. Imaging of multiples. (a) The 5th iteration of LSM with a crosscorrelation imaging condition, (b) the 20th iteration of LSM with a crosscorrelation imaging condition, (c) the 5th iteration of LSM with a deconvolution imaging condition, and (d) the image residual during inversion.

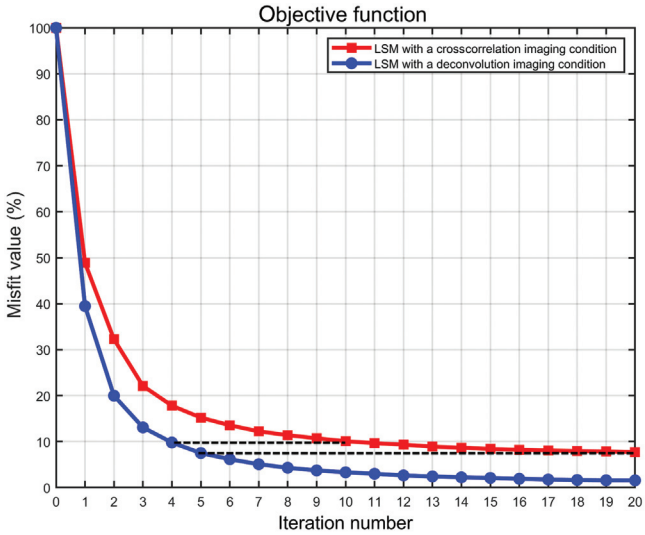

Figure 10. Objective function of LSM with a crosscorrelation imaging condition (red) versus that of LSM with a deconvolution imaging condition (blue).

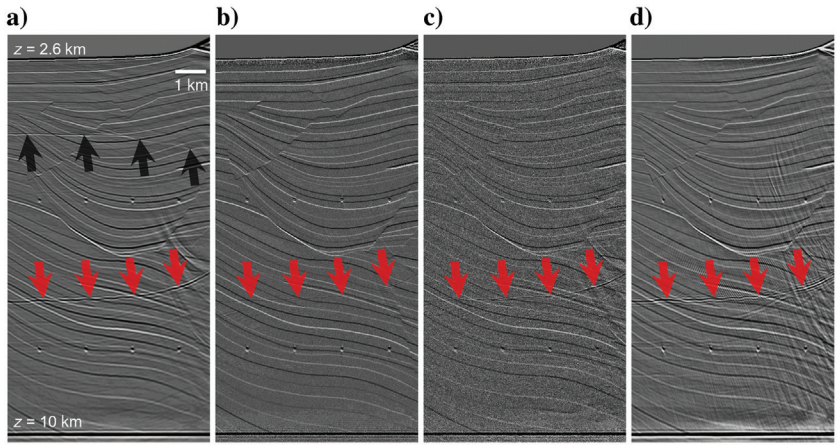

Figure 11. Imaging of multiples with (a) a crosscorrelation imaging condition, (b) LSM with noise in the input data (noise level = 10% of the data amplitude), (c) LSM with noise in the input data (noise level = 20% of the data amplitude), and (d) LSM with noninverse crime data as the input.

CONCLUSION

We investigate the imaging of multiples with different crosstalk attenuation strategies. First, we propose an approach to identify and predict crosstalk events in the image domain based on their causality. Then, we mathematically derive the effects of a deconvolution imaging condition on crosstalk attenuation and demonstrate that it improves the signal-to-noise ratio and suppresses the crosstalk amplitudes. Moreover, we demonstrate that LSM removes crosstalk events iteratively. Finally, to speed up the LSM of multiples, we propose a strategy that combines a deconvolution imaging condition with a fast LSQR solver. By applying the fast LSM method to the Sigsbee2b data set, we reduce the cost function by 90% within five iterations while removing most of the crosstalk.

Overall, among all algorithms available to attenuate the crosstalk generated during the imaging of multiples, migration with a deconvolution imaging condition is the most practical approach and can be used in certain scenarios when the multiples are not too strong. Although a deconvolution imaging condition cannot completely address the crosstalk issue, it can effectively attenuate short-period crosstalk events. In addition, a deconvolution imaging condition is easy to implement without impacting the computational cost. LSM combined with a deconvolution imaging condition and a fast LSQR solver turns out to be an optimal strategy to attenuate crosstalk and converge rapidly.

ACKNOWLEDGMENTS

The authors would like to thank the reviewers for their comments and suggestions. In particular, we want to thank the assistant editor, A. Guitton, for his careful editing and constructive suggestions, which significantly improved the paper. This study is partially funded by the National Natural Science Foundation of China (grant no. 42074123), the Pearl River Talent Program of Guangdong, China (grant no. 2017ZT07Z066) and the National Natural Science Foundation of China (grant no. 11971258).

DATA AND MATERIALS AVAILABILITY

Data associated with this research are available and can be obtained by contacting the corresponding author.

APPENDIX A

IMAGING CONDITION AND WAVE-EQUATION MIGRATION

The crosscorrelation imaging condition (equation A-1) and the deconvolution imaging condition (equation A-2) can be written, respectively, as

$$I_{\text{corr}} = \sum_{\omega}\left[\left(G_s\sum_j S_j\right)^*\left(G_r\sum_l R_l\right)\right], \tag{A-1}$$

$$I_{\text{decon}} = \sum_{\omega}\frac{\left(G_s\sum_j S_j\right)^*\left(G_r\sum_l R_l\right)}{\left(G_s\sum_j S_j\right)^*\left(G_s\sum_j S_j\right)}, \tag{A-2}$$

where ω is the temporal frequency; I_{corr} and I_{decon} are the migrated images based on the crosscorrelation and deconvolution imaging conditions, respectively; G_s and G_r are the frequency-domain Green's functions; and S and R are the frequency-domain-transformed source and receiver wavefields, respectively.

To compute the wavefield in $v(z)$ media, we solve the following acoustic wave equation:

$$\frac{\partial^2 P(\mathbf{x},t)}{\partial t^2} - v^2\nabla^2 P(\mathbf{x},t) = 0, \tag{A-3}$$

where P is the pressure wavefield. By applying the Fourier transform in time, we obtain the Helmholtz equation

$$\nabla^2 P(x,\omega) + k^2 P(x,\omega) = 0, \tag{A-4}$$

where $k = \omega/v$ is the wavenumber. Equation A-4 can be factorized as (Claerbout, 1985)

$$\left(\frac{\partial}{\partial z} - i\sqrt{k^2 + \partial^2/\partial x^2}\right)\left(\frac{\partial}{\partial z} + i\sqrt{k^2 + \partial^2/\partial x^2}\right)P(x,\omega) = 0. \tag{A-5}$$

Then, the solution to equation A-5 can be written as (Gazdag, 1978; Gazdag and Sguazzero, 1984)

$$P(x,\omega) = S_0 \exp(\pm i k_z z), \tag{A-6}$$

where $k_z = \sqrt{k^2 + \partial^2/\partial x^2}$ is the vertical component of the wavenumber, and S_0 can be the source wavefield at zero depth. In equation A-6, the negative and positive signs correspond to forward and backward propagation, respectively.

APPENDIX B

CROSSTALK ATTENUATION WITH THE DECONVOLUTION IMAGING CONDITION

We explicitly decompose equation 15. Based on the causal and anticausal crosstalk analysis, the numerator of this equation contains three components:

$$S_0^2\sum_j m^{2j+1} + S_0^2 I_c + S_0^2 I_a = I_0 + I_{\text{causal}} + I_{\text{a-causal}}, \tag{B-1}$$

where I_{causal} and $I_{\text{a-causal}}$ are the causal and anticausal crosstalk terms, respectively, and

$$\begin{aligned} I_0 &= S_0^2\sum_j m^{2j+1}, \\ I_{\text{causal}} &= S_0^2 I_c, \\ I_{\text{a-causal}} &= S_0^2 I_a, \end{aligned} \tag{B-2}$$

with

$$\begin{aligned} I_c &= \sum_{j\geq 0}\sum_{l>j+1}(-1)^{j+l-1} m^{j+l}\exp[(-ik_z)2(l-(j+1))z], \\ I_a &= \sum_{j>0}\sum_{l\leq j}(-1)^{j+l-1} m^{j+l}\exp[(-ik_z)2(l-(j+1))z]. \end{aligned} \tag{B-3}$$

Similarly, the denominator of equation 15 can be decomposed as

$$\begin{aligned} &S_0^2\sum_j m^{2j} + S_0^2 I_d \\ &= \sum_j\sum_l (-1)^{j+l} m^{j+l} S_0^2 \exp[(-ik_z)2(l-j)z] \\ &= S_0^2\sum_j m^{2j} + \sum_j\sum_{l\neq j}(-1)^{j+l} m^{j+l} S_0^2 \exp[(-ik_z)2(l-j)z] \\ &= S_0^2\sum_j m^{2j} + S_0^2 I_d, \end{aligned} \tag{B-4}$$

where

$$I_d = \sum_j\sum_{l\neq j}(-1)^{j+l} m^{j+l}\exp[(-ik_z)2(l-j)z]. \tag{B-5}$$

Then, the deconvolution imaging condition can be written as

$$I_{\text{decon}} = \sum_\omega \frac{S_0^2\sum_j m^{2j+1} + S_0^2 I_c + S_0^2 I_a}{S_0^2\sum_j m^{2j} + S_0^2 I_d} \approx m + \sum_\omega \frac{A_0}{1+B_0}, \tag{B-6}$$

where

$$\begin{aligned} A_0 &= \frac{I_c + I_a}{\sum_j m^{2j}}, \\ B_0 &= \frac{I_d}{\sum_j m^{2j}}. \end{aligned} \tag{B-7}$$

REFERENCES

Berkhout, A. J., 2014, An outlook on the future of seismic imaging — Part 2: Full-wavefield migration: Geophysical Prospecting, **62**, 931–949, doi: 10.1111/1365-2478.12154.

Berkhout, A. J., and D. J. Verschuur, 1994, Multiple technology — Part 2: Migration of multiple reflections: 64th Annual International Meeting, SEG, Expanded Abstracts, 1497–1500, doi: 10.1190/1.1822821.

Claerbout, J. F., 1971, Toward a unified theory of reflector mapping: Geophysics, **36**, 467–481, doi: 10.1190/1.1440185.

Claerbout, J. F., 1985, Imaging the earth's interior: Blackwell Scientific Publications, 414.

Davydenko, M., and D. J. Verschuur, 2016, Full-wavefield migration: Using surface and internal multiples in imaging: Geophysical Prospecting, **65**, 7–21, doi: 10.1111/1365-2478.12360.

Gazdag, J., 1978, Wave equation migration with the phase-shift method: Geophysics, **43**, 1342–1351, doi: 10.1190/1.1440899.

Gazdag, J., and P. Sguazzero, 1984, Migration of seismic data by phase shift plus interpolation: Geophysics, **49**, 124–131, doi: 10.1190/1.1441643.

Guitton, A., A. Valenciano, D. Bevc, and J. Claerbout, 2007, Smoothing image condition for shot-profile migration: Geophysics, **72**, no. 3, S149–S154, doi: 10.1190/1.2712113.

Liu, Y., X. Chang, D. Jin, R. He, H. Sun, and Y. Zheng, 2011, Reverse time migration of migration of multiples for subsalt imaging: Geophysics, **76**, no. 5, WB209–WB216, doi: 10.1190/geo2010-0312.1.

Liu, Y., X. Liu, A. Osen, Y. Shao, H. Hu, and Y. Zheng, 2016, Least-squares reverse time migration using controlled-order multiple reflections: Geophysics, **81**, no. 5, S347–S357, doi: 10.1190/geo2015-0479.1.

Lu, S., F. Liu, N. Chemingui, and M. Orlovich, 2018b, Full-wavefield migration by inversion: 88th Annual International Meeting, SEG, Expanded Abstracts, 4311–4315, doi: 10.1190/segam2018-2995120.1.

Lu, S., F. Liu, N. Chemingui, A. Valenciano, and A. Long, 2018a, Least-squares full-wavefield migration: The Leading Edge, **37**, 46–51, doi: 10.1190/tle37010046.1.

Lu, S., D. N. Whitmore, A. A. Valenciano, and N. Chemingui, 2015, Separated-wavefield imaging using primary and multiple energy: The Leading Edge, **34**, 770–778, doi: 10.1190/tle34070770.1.

Lu, S., N. Whitmore, A. Valenciano, N. Chemingui, and G. Ronholt, 2016, A practical crosstalk attenuation method for separated wavefield imaging: 86th Annual International Meeting, SEG, Expanded Abstracts, 4235–4239, doi: 10.1190/segam2016-13849878.1.

Muijs, R., J. O. Robertsson, and K. Holliger, 2007, Prestack depth migration of primary and surface-related multiple reflections — Part 2: Identification and removal of residual multiples: Geophysics, **72**, no. 2, S71–S76, doi: 10.1190/1.2424544.

Ordoñez, A., W. Söllner, T. Klüver, and L. J. Gelius, 2014, Migration of primaries and multiples using an imaging condition for amplitude-normalized separated wavefields: Geophysics, **79**, no. 5, S217–S230, doi: 10.1190/geo2013-0346.1.

Paffenholz, J., B. Mclain, J. Zaske, and P. J. Keliher, 2002, Subsalt multiple attenuation and imaging: Observations from the Sigsbee2B synthetic data set: 72nd Annual International Meeting, SEG, Expanded Abstracts, 2122–2125, doi: 10.1190/1.1817123.

Paige, C. C., and M. A. Saunders, 1982, LSQR: An algorithm for sparse linear equations and sparse least squares: ACM Transactions on Mathematical Software, **8**, 43–71, doi: 10.1145/355984.355989.

Ravasi, M., I. Vasconcelos, A. Kritski, A. Curtis, C. da Costa Filho, and G. A. Meles, 2016, Target-oriented Marchenko imaging of a North Sea field: Geophysical Journal International, **205**, 99–104, doi: 10.1093/gji/ggv528.

Schuster, G. T., and J. Rickett, 2000, Daylight imaging in *V(x, y, z)* media. Utah tomography and modeling-migration: Project midyear report, 55-66.

Shan, G., 2003, Source-receiver migration of multiple reflections: 73rd Annual International Meeting, SEG, Expanded Abstracts, 1008–1011, doi: 10.1190/1.1817440.

Tu, N., A. Aravkin, T. van Leeuwen, and F. Herrmann, 2013, Fast least-squares migration with multiples and source estimation: 75th Annual International Conference and Exhibition, EAGE, Extended Abstracts, 348-00260, doi: 10.3997/2214-4609.20130727.

Valenciano, A. A., and B. Biondi, 2003, 2-D deconvolution imaging condition for shot-profile migration: 73rd Annual International Meeting, SEG, Expanded Abstracts, 1059–1062, doi: 10.1190/1.1817454.

Verschuur, D. J., 1991, Surface-related multiple elimination: An inversion approach: Ph.D. thesis, Delft University of Technology.

Wang, Y., Y. Zheng, L. Zhang, X. Chang, and Z. Yao, 2014, Reverse time migration of multiples: Eliminating migration artifacts in angle domain common image gathers: Geophysics, **79**, no. 6, S263–S270, doi: 10.1190/geo2013-0441.1.

Wapenaar, K., J. Thorbecke, J. van ver Neut, F. Broggini, E. Slob, and R. Snieder, 2014, Marchenko imaging: Geophysics, **79**, no. 3, WA39–WA57, doi: 10.1190/geo2013-0302.1.

Wong, M., B. Biondi, and S. Ronen, 2015, Imaging with primaries and free-surface multiples by joint least-squares reverse time migration: Geophysics, **80**, no. 6, S223–S235, doi: 10.1190/geo2015-0093.1.

Zhang, D., and G. T. Schuster, 2014, Least-squares reverse time migration of multiples: Geophysics, **79**, no. 1, S11–S21, doi: 10.1190/geo2013-0156.1.

Zhang, Y., G. Zhang, and N. Bleisten, 2005, Theory of true amplitude one-wave wave equations and true amplitude common-shot migration: Geophysics, **70**, no. 4, E1–E10, doi: 10.1190/1.1988182.

Biographies and photographs of the authors are not available.